ADVANCED FUNCTIONAL MATERIALS
www.afm-journal.de

Shape-Reconfigurable Crack-Based Strain Sensor with Ultrahigh and Tunable Sensitivity

*Seungjae Lee, Youngoh Lee, Cheolhong Park, Yun Goo Ro, Min Sub Kwak, Geonyoung Jeong, Junseo Park, Hyejin Lee, Pan Kyeom Kim, Sung-Il Chung, and Hyunhyub Ko**

In the field of wearable electronics and human–machine interfaces, there is a growing need for highly sensitive and adaptable sensors capable of detecting a wide range of stimuli with high precision. Traditional sensors often lack the versatility to adjust their sensitivity for different applications. Inspired by the mechanosensory system of spiders, a shape-reconfigurable crack-based sensor with ultrahigh and tunable strain sensitivity based on the precise control of nanocrack formation on a shape memory polymer substrate is demonstrated. This design incorporates a line-patterned substrate composed of a thermoplastic polyurethane (TPU) matrix and thermo-responsive shape memory polymer, poly(lactic acid) (PLA), to form parallel nanocracks in a thin platinum film. This design achieves an ultrahigh gauge factor of 2.7×10^9 at 2% strain, significantly surpassing conventional sensors. The shape memory property of the TPU/PLA substrate enables tunable strain sensitivity according to the desired strain range, eliminating the need for multiple sensors. The sensor demonstrates exceptional capabilities in detecting subtle strains (as low as 0.025%), monitoring biological signals, and sensing acoustic waves (100–20 000 Hz) with a response time of 0.025 ms. This work represents a significant advancement toward strain sensors with both ultrahigh and tunable sensitivity.

1. Introduction

The rapid growth of wearable electronics has driven the development of flexible physical sensors, revolutionizing various fields including healthcare monitoring,[1,2] augmented or virtual reality (AR/VR),[3,4] and human–machine interfaces. These sensors, used for bio-signal,[5,6] motion,[7,8] and sound[9,10] detection, are driving the exploration of innovative approaches in sensor design and functionality. Such applications often require the ability to detect highly precise and minute mechanical deformations, which play a critical role in both biomedical and acoustic systems. In biomedical contexts, fine deformations caused by physiological signals such as pulse, respiration, and cardiac activity are essential for accurate health monitoring and early detection of abnormalities.[11–13] Similarly, micrometer-scale deformations from tumor growth or vocal cord vibrations are vital for cancer diagnostics and voice recognition technologies.[14,15] These examples highlight the importance of sensors capable of reliably detecting minute changes, demonstrating their indispensability in advancing healthcare and acoustic sensing technologies.

To enhance sensor capabilities, researchers are investigating bio-inspired approaches, mimicking nature's distinctive properties and sensory functions. This approach has led to the development of various sensor structures, each emulating specific natural structures. Examples include interlocked ridge structures,[16,17] hierarchical structures,[18,19] finger patterns,[20] and whiskers,[21,22] each emulating structures found in human skin, sea-urchin, fingerprint, and hairy structures of mammals, respectively. These biomimetic designs have significantly advanced flexible sensors, enabling more precise and multifaceted sensing capabilities. Particularly noteworthy are crack-based strain sensors, inspired by the crack-shaped slit structure of arthropods' mechanosensory system.[15,23–27] These sensors utilize the principle that cracks in conductive materials can significantly alter electrical pathways under strain, resulting in highly sensitive strain detection.

However, despite their sensitivity, efforts to expand the detection range to stimuli from subtle biological signals to large body movements often come at the cost of reduced sensitivity to small deformations.[28–30] While recent studies have reported various approaches to control crack formation, maintaining consistent sensitivity in the low strain regime remains a challenge, especially when applied to on-skin environments.[31–36] The introduction of interface layers and mechanical coupling with the skin

S. Lee, Y. Lee, C. Park, Y. G. Ro, M. S. Kwak, G. Jeong, J. Park, H. Lee, H. Ko
School of Energy and Chemical Engineering
Ulsan National Institute of Science and Technology (UNIST)
50 UNIST-gil, Ulsan 44919, Republic of Korea
E-mail: hyunhko@units.ac.kr
P. K. Kim, S.-I. Chung
Nano Hybrid Technology Research Center
Korea Electrotechnology Research Institute
Miryang 50463, Republic of Korea

The ORCID identification number(s) for the author(s) of this article can be found under https://doi.org/10.1002/adfm.202421812

DOI: 10.1002/adfm.202421812

can significantly affect strain transfer efficiency. Although advanced designs have achieved detection limits as low as 0.05%–0.1%, irregular crack distribution and persistent electrical connections under slight deformation compromise sensitivity. This limitation significantly affects the detection of fine physiological signals or minute movements, which are crucial for practical applications requiring robust and precise monitoring in real-world conditions.

Furthermore, conventional sensors with fixed sensitivity face limitations in accurately detecting stimuli outside their most sensitive range. This lack of adaptability is a significant drawback in applications requiring responsiveness to varying strain intensities or different stimulus types. For instance, a sensor optimized for subtle skin deformations might not be suitable for larger joint movements without recalibration. This challenge underscores the need for sensors with tunable sensitivities optimized for different stimuli within a single device. Recent research has demonstrated various methods for achieving tunable sensitivities. Arias et al. developed a method of adjusting the surface wettability of polymer substrates, affecting crack evolution in thin-metal based crack sensors.[37] Carbon-based nanomaterials have also been utilized in crack-based strain sensors, with sensitivity tuning achieved by varying laser intensity during polyimide pyrolysis[38] or adjusting current in graphene electrical breakdown.[39] While promising, these methods often require multiple sensors for various target stimuli, as they do not enable sensitivity tuning within a single sensor. This limitation can increase complexity and cost in applications requiring detection of multiple strain ranges or stimulus types. Inspired by spiders' ability to tune their sensing capabilities through slit manipulation, Kang et al. developed a mechanosensor with tunable sensitivity by applying preset strain, achieved through a 3D-printed frame with adjustable spacing.[40] Although useful for healthcare applications, the frame-based design limits the sensor's capabilities. The thin-film sensor between the frames lacks mechanical stability, and the rigid frame restricts flexibility and large deformations. These limitations highlight the need for frameless sensor designs that offer tunable sensitivity, particularly for applications requiring high flexibility and unrestricted placement. Current research faces significant challenges in achieving ultrahigh sensitivity while maintaining control over sensitivities within a single sensor. For wearable electronics, simpler methods to tune sensitivities within individual sensors are essential. The ideal solution would be a sensor capable of dynamically adjusting its sensitivity range without separate structural components or complex fabrication, providing versatile and adaptable performance in a single device.

To address the aforementioned issues, we propose a shape-reconfigurable strain sensor with ultrahigh and tunable sensitivity based on precise nanocrack control on a shape memory substrate. This design significantly enhances sensitivity through uniform patterned cracks and allows effective sensitivity tunability within a single sensor using an adaptive shape memory polymer (SMP). Our Shape-Memory Adaptive Crack-based Sensitivity-Tunable Sensor (SMARTS) can detect subtle strain changes with ultrahigh sensitivity and adjust its sensitivity for selective strain detection. Our approach comprises two key innovations. First, to significantly enhance sensitivity to subtle strain, we fabricated a strain sensor with uniformly patterned parallel cracks by introducing a line pattern, enabling precise control of nanocrack formation (**Figure 1a**). This line pattern structure effectively concentrates strain-induced stress along the lines, leading to the formation of parallel line cracks (Figure 1b), enabling ultrahigh sensitivity. Second, for effective sensitivity tunability within a single sensor, we incorporated an SMP into the stretchable substrate. SMPs can be programmed into temporary shapes and recover their original shape in response to heat, allowing the parallel line cracks on the shape memory substrate to be reconfigured. The shape memory effect-induced preset strain enables control of initial crack gap distance, facilitating rapid sensor response to applied mechanical stimuli (Figure 1c). In this system, net points serve as fixed anchors that maintain the material's structural stability, while molecular switches enable the reversible transitions between temporary and original shapes, driving the reconfiguration of crack geometries. Compared with previously studied crack-based strain sensors, our SMARTS demonstrates ultrahigh sensitivity to subtle changes and can tune its sensitive ranges, enabling selective stimuli detection (Figure 1c). This work represents the first proof-of-concept showing that shape memory polymers can enable dynamic sensitivity control without relying on a frame. This frameless approach opens new possibilities for sensitivity tuning across a broader range of sensor designs, particularly where unrestricted deformation and flexibility are essential.

2. Results and Discussion

2.1. Line-Patterned Parallel Line Cracks for Ultrahigh Sensitivity

Cracks form to release the stress applied to the metal/polymer system when the strain exceeds the critical strain value of the system.[41] Cracks in the conductive metal film remain closed without strain; however, as the applied strain increases, these cracks open, disrupting the conductive path and resulting in a change in resistance. The extent to which the cracks open varies with the magnitude of the applied strain, causing a change in resistance and enabling the film to function as a strain sensor. Previous crack sensors with a broad detectable range exhibited relatively low sensitivity in the low strain range, facing constraints in detecting subtle stimuli or vibrations.[31–36,42] While sensors with tunable sensitivities offer high sensitivity in the low strain range, they often require integrating multiple sensors with different sensitivities for various target stimuli.[37–39,43] Therefore, a new method for simply tuning the sensitivity within a single sensor is required.

To overcome the limitations of existing crack-based sensors and achieve both high sensitivity and tunability in a single device, we designed a shape-reconfigurable crack-based strain sensor based on regular cracks on a shape memory substrate with nanoscale line patterns (Figure 1a). A line pattern (width/pitch/height = 400/800/≈55 nm) was incorporated on the substrate to facilitate precise and regular formation of parallel cracks. Contrast to traditional methods, which are limited by their resolution for cracks, or use microscale patterns as crack structures themselves rather than systematically generating nanocracks, our approach enables precise control over crack formation, ensuring uniformity and reproducibility.[44,45] In addition, thermo-responsive SMP was incorporated in the substrate to tune the sensitivity within a single sensor by reconfiguring

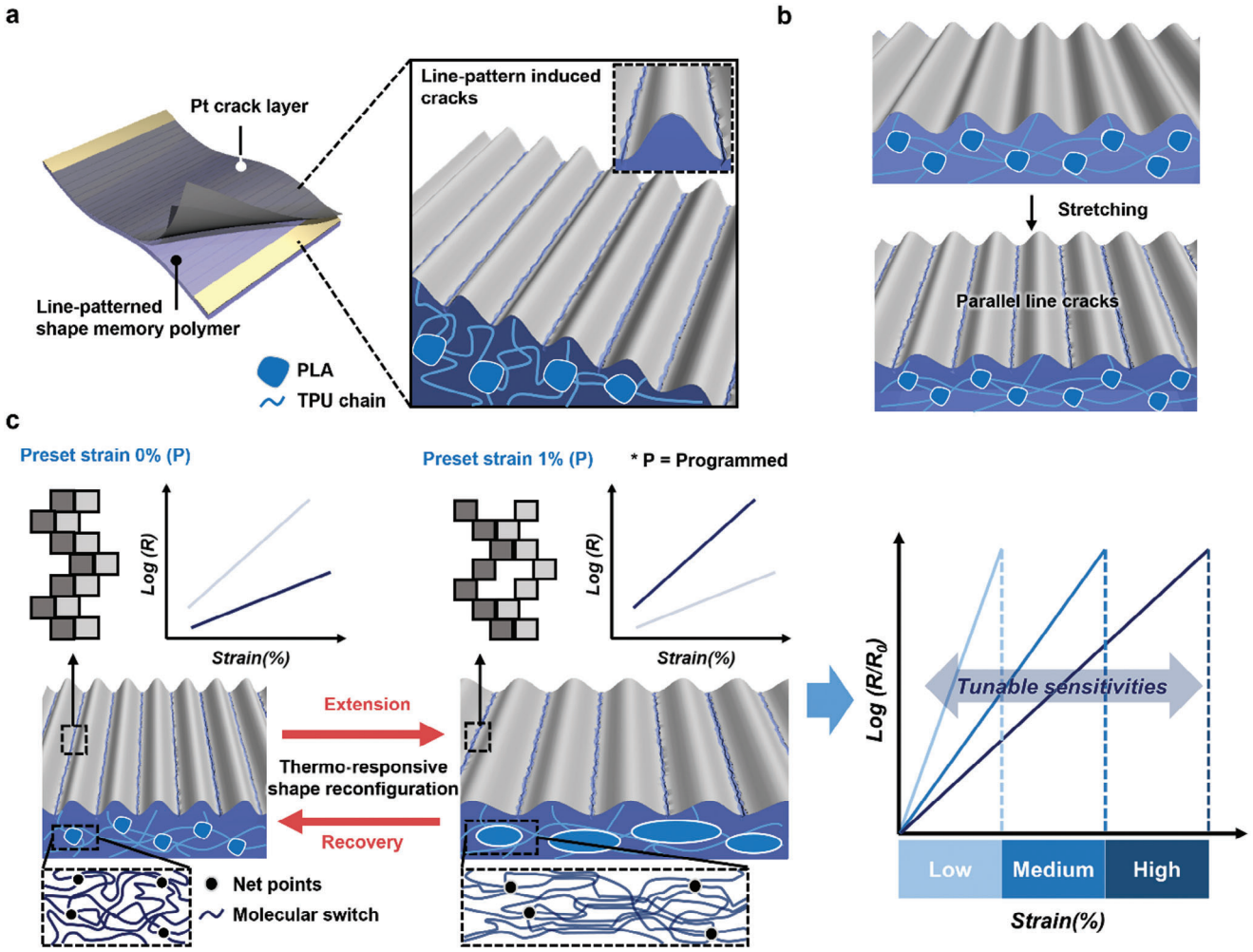

Figure 1. Conceptual illustration of the shape-reconfigurable crack-based sensor with ultrahigh and tunable sensitivity. a) Schematic illustration of the line-patterned crack sensor based on a TPU/PLA substrate with line pattern and thin Pt film. The expanded view reveals uniformly located cracks along the line pattern-guided structure. The polymer network consists of TPU chains and PLA particles. b) Mechanism for crack formation: lateral stretching induces stress concentration along the line patterns, resulting in uniform parallel cracks perpendicular to the strain direction. c) Mechanism of sensitivity tuning through thermo-responsive shape reconfiguration: shape memory effect of PLA/TPU substrate controlling initial crack gaps through preset strain conditions (left). The PLA structure comprises net points (black dots) serving as physical cross-links that maintain the permanent shape of the polymer, and molecular switch (blue wavy lines), which facilitate controlled deformation and shape recovery. These elements determine the initial density of conductive pathways. Higher preset strain creates wider crack gaps with fewer conductive pathways, leading to amplified resistance changes rapidly even under lower strain range, as demonstrated in resistance–strain curves with different sensitivity ranges (right).

the initial cracks in response to temperature changes, thereby effectively controlling the ranges of highest sensitivity. To significantly enhance the sensitivity, we employed line patterns to ensure uniform and precise formation of regular parallel line cracks through directed stress concentration along the line pattern, facilitating controlled crack development (Figure 1b). The stretchable SMARTS is based on a line-patterned substrate composed of a thermoplastic polyurethane (TPU) matrix and thermo-responsive shape memory polymer, poly(lactic acid) (PLA). TPU was chosen as the substrate for composites with PLA due to its excellent elasticity, mechanical durability, and compatibility with solution-based processing. When comparing polycaprolactone (PCL)/TPU and PLA/TPU composites, PCL/TPU often exhibited surface wrinkling and permanent deformation during prestretching, making it difficult to fabricate devices with uniform cracks. In contrast, PLA/TPU composites demonstrated stable crack formation due to PLA's high stiffness and controlled plastic deformation, making it the optimal choice. The film was subsequently coated with Pt via sputtering, and then prestretched to induce the uniform formation of parallel line cracks in the Pt layer across the film (Figure S1, Supporting Information).

To understand the mechanism behind the enhanced sensitivity of our line-patterned strain sensor, we conducted finite-element analysis (FEA) simulation comparing stress distributions in planar and line-patterned structures under strain (**Figure 2a**). FEA revealed that stress was evenly distributed over the surface in a planar structure, aligning with previous study that stress in thin films is uniformly distributed when their thickness is much smaller than their lateral dimensions.[46] This result suggests that even minor surface defects could

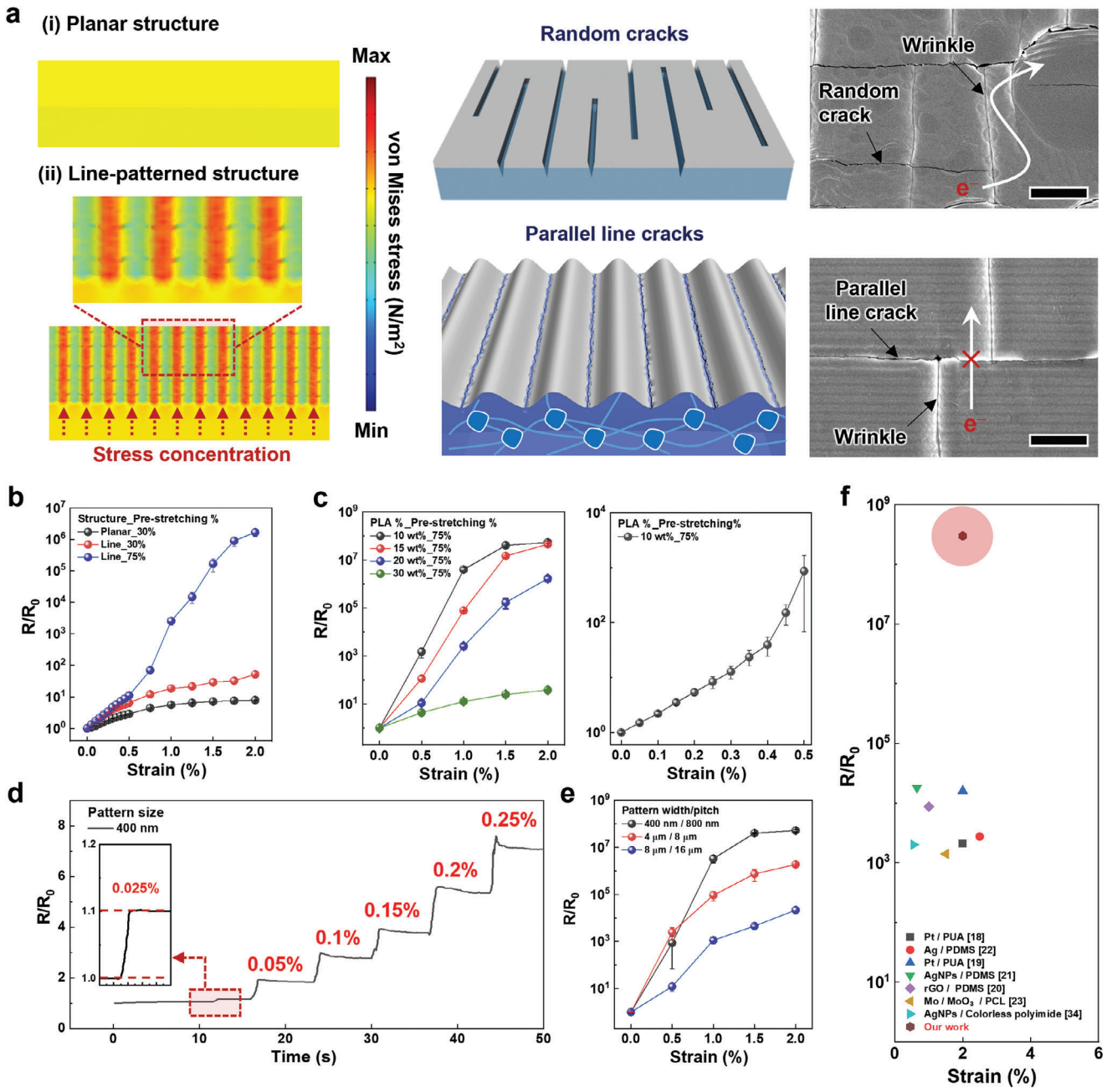

Figure 2. Line pattern-guided crack formation for ultrasensitive and controllable strain sensing. a) FEA simulation showing structural effect on crack formation: i) Random crack formation on planar structure due to unexpected stress concentration around surface defects, resulting in continuous conductive paths. ii) Parallel line crack formation induced by line-patterned structure, effectively concentrating strain stress along pattern valleys and disrupting conductive paths. b) Comparison of strain sensitivity for sensors with and without line patterns depending on prestretching %. c) Effect of PLA concentration in the TPU/PLA substrate on strain sensitivity. d) Stepwise strain sensing performance, showing the detection of small and incremental changes in strain. e) Influence of line pattern size on sensor performance. f) Comparison of strain sensitivities with previously reported crack-based strain sensors.

concentrate stress, leading to stress release at random spots and resulting in nonuniform and randomly oriented crack formation (Figure 2a(i)). Random cracks maintain continuous conductive pathways under tensile strain, leading to smaller resistance changes (ΔR) with strain (ε). Since the sensitivity of a strain sensor, measured by the gauge factor (GF = $(\Delta R/R_0)/\varepsilon$), is proportional to resistance changes, continuous conductive pathways reduce the sensitivity to subtle changes. Conversely, with a parallel line pattern, stress was concentrated along the lines on the substrate, leading to more uniform parallel crack formation compared to a planar structure (Figure 2a). This result indicates that line patterns can effectively guide crack formation. Compared

to the planar one, the creation of parallel line cracks along the pattern that cut entirely through the film breaks the conductive pathways, resulting in ultrahigh sensitivity to subtle changes (Figure 2a and Figure S2, Supporting Information). To validate the effect of introducing a parallel line pattern, we compared the GF values of strain sensors without (Black) and with the line pattern (Red). Our experimental results showed a 225% increase in the relative resistance (R/R_0) for the line-patterned sensor compared to the planar sensor under 2% strain (Figure 2b). This enhancement was attributed to effective stress concentration along the line pattern, which induced the more uniform formation of parallel cracks, resulting in efficient breakage of conductive pathways in response to strain. The role of stress concentration in guiding crack formation is further supported by previous research. Stress concentration on uneven surface geometry has been well-documented[47,48] and previous studies have shown that tensile stress can be concentrated along the edges of structures, controlling crack formation.[49]

To further elucidate the impact of line patterns on crack formation, we conducted detailed morphological analyses using surface scanning electron microscopy (SEM) and atomic force microscopy (AFM), respectively (Figures S3 and S4, Supporting Information). In the absence of line patterns, although parallel cracks form perpendicular to the tensile strain, they are often discontinuous along their length. These discontinuities maintain conductive pathways, allowing current to flow even when the cracks open (Figure S3a, Supporting Information, red boxes and arrow lines). These persistent conductive pathways limit the reduction in overall conductivity with the increase of strain, resulting in reduced sensitivity to tensile strain. In contrast, the line-patterned structure guides crack formation along the edges of line patterns, creating continuous parallel line cracks. These uninterrupted cracks effectively block current paths when they open under strain, leading to an immediate increase in resistance even at lower strain ranges. When no strain is applied to the line-patterned sensor, conductive pathways form at the adjacent crack edges in the overlapping regions (blue box), enabling tunneling currents[17,38] (Figure S3b, Supporting Information). The quantitative analysis of crack density (Figure S3c, Supporting Information) confirms that line-patterned structures produce a higher and more uniform crack density (0.065/μm) compared to the planar structures (0.038/μm). This increase is attributed to the line pattern effectively concentrating stress along its geometric features, facilitating the formation of numerous parallel cracks. The controlled crack density in the patterned structures ensures a consistent response to tensile strain, resulting in enhancement of sensing performance.

Furthermore, AFM analysis (Figure S4, Supporting Information) revealed that the irregular surface structure of planar substrates results in nonuniform stress distribution. This uneven stress distribution causes significant variations in crack depth on planar surfaces, with some regions exhibiting deeper cracks due to localized stress intensification (Black dotted box, Figure S4a, Supporting Information), while other regions maintain conductive pathways due to insufficient crack formation (Red arrows, Figure S4a, Supporting Information). These conductive regions limit the extent of resistance change under applied strain, thereby reducing the sensitivity of the planar structure. In contrast, line-patterned structures enable stress concentration along the patterned ridges, guiding crack propagation in a more uniform manner. These guided cracks propagate continuously along the edges of the line patterns without interruptions and exhibit greater average depth compared to the discontinuous and shallower cracks observed in planar structures, as demonstrated in Figure S4b (Supporting Information). The increased depth of cracks in line-patterned structures (≈95.6 nm) compared to planar structure (≈84.5 nm) further enhances the resistance change with applied strain, contributing to their higher sensitivity (Figure 2a and Figure S4c, Supporting Information). Metal-film-based crack sensors exhibit varying crack formations depending on the metal deposition method. We optimized the metal deposition conditions by comparing metal types and sputtering times, which influence crack formation and metal thickness, respectively. Compared to other metals and deposition methods (Figures S5 and S6 and as detailed in Note S2, Supporting Information), platinum films deposited by sputtering form denser and more uniform layers with higher compressive stress. This uniformity allows cracks to propagate more consistently through the evenly stressed material, resulting in straighter crack patterns (Figure S3, Supporting Information), even without additional surface modification. Among the various metals and deposition methods we tested, Pt sputtering demonstrated the most consistent crack formation and reliable sensor performance (Figure S7, Supporting Information). Thus, we chose Pt sputtering on a PLA/TPU substrate as the optimal approach for the final sensor fabrication.

We investigated parameters affecting the sensitivity of the sensor. Cracks typically form due to stress release induced by surface defects during simultaneous prestretching of both the rigid metal and stretchable substrate.[40,41] Previous research has shown that sensitivity can be affected by factors such as crack density, surface roughness, and stress concentration effectiveness.[23,24] Crack formation primarily depends on the percentage of prestretching. As this percentage increases, sensitivity improves (Figure 2a), attributed to the higher crack density. Optical images confirm that increased prestretching leads to more cracks per unit length (Figure S8, Supporting Information). Higher crack density, analogous to more resistances in an electrical circuit, results in reduced electrical conductance under strain.

Surface roughness and morphology can affect the crack formation. Since we incorporated PLA, a thermo-responsive shape memory polymer, into the stretchable TPU, the effect of PLA concentration on the sensitivity was examined. Figure 2c shows that increased PLA concentration decreased sensitivity, attributed to crack asperity. OM and cross-sectional SEM images (Figures S9a and S10a, Supporting Information) reveal variations with PLA concentration. Higher PLA concentrations resulted in larger, and more spherical domains on the film surface. Raman spectroscopy confirmed that the spherical domains were dispersed PLA particles embedded within the TPU matrix consistent with the PLA dispersion in TPU matrix (Figure S10b, Supporting Information).[50] Consequently, when strain was applied, stress was concentrated not only along the line patterns, but also around the PLA spherical particles due to surface imperfections. In regions with lower PLA concentrations (e.g., 10 and 15 wt%) (the upper section in Figure S9a, Supporting Information), uniformly parallel line cracks are predominantly observed due to the minimal influence of PLA particles. The behavior of these parallel line cracks during stretching is illustrated in Figure S9b(i)

(Supporting Information). As the cracks open, the few conductive points along the line cracks cause large resistance changes, resulting in high sensitivity. In contrast, higher PLA concentrations (e.g., 20 and 30 wt%) (the lower section in Figure S9a, Supporting Information) result in the formation of tortuous cracks around PLA particles due to localized stress distributions. As shown in Figure S9b(ii) (Supporting Information), the greater number of conductive points in these tortuous cracks ensures better electrical connectivity during stretching, which enhances electrical conductance but leads to lower sensitivity compared to line cracks. This reconnection maintains electrically conductive points and may even increase electrical conductance (Figure S9b(ii), Supporting Information).[23] We leveraged this property to control strain sensitivities based on PLA concentration. Lower PLA concentrations enhance sensitivity to subtle tensile strain changes, whereas higher concentrations are beneficial for detecting larger strains. At low PLA concentration, the line pattern dominates, generating parallel line cracks, resulting in high sensitivity at low strain ranges. As PLA concentration increases, more and larger circular domains create additional stress concentration points, allowing simultaneous crack formation induced by both line patterns and PLA circular domains. In addition, the stress distribution around PLA domains becomes more pronounced, disrupting the uniform response of the composite under strain (Figure S11, Supporting Information). It could disrupt the uniform crack propagation along the line patterns during subtle tensile strain, leading to irregular crack propagation that do not fully align with the applied strain direction. As a result, the electrical resistance change becomes less pronounced, and the sensor's sensitivity reduces.

Through balancing several parameters, the line-patterned crack sensor with PLA 10 wt% under prestretching 75% achieves an ultrahigh GF of 2.7×10^9 at 2% strain (Figure S12, Supporting Information), and the ultrahigh sensitivity of the line-patterned crack sensor allows detection of small, stepwise loadings of 0.05% strain (Figure 2c,d) and a minimum detectable strain of 0.025% strain with high sensitivity (GF $\cong$ 400) (Figure 2d). These results are attributed to the high quality of crack formation guided by the nanoscale line pattern. A slight decrease in resistance at 0.25% strain is observed, attributed to elastic recovery properties of the polymer composite. Furthermore, tensile stress–strain curves showed negligible hysteresis within the working range (<2%), ensuring reliable sensor operation during loading and unloading (Figure S13, Supporting Information). In addition, the line pattern size affects sensitivity. FEA simulations were conducted to analyze the effects of pattern dimensions on crack formation (Figure S14, Supporting Information). Initially, the pattern width was increased while maintaining the same height (50 nm) as the nanopatterns. However, this caused the structure to resemble a planar surface, significantly reducing the effectiveness of stress concentration. To address this, both the width and height of the patterns were increased, which resulted in consistent crack formation along the grooves regardless of depth. This confirmed that stress concentration along the pattern grooves, rather than depth itself, is the critical factor for crack formation. For various micro-sized line patterns (width/pitch/height = 4/8/0.6, 8/16/1.5 μm), SEM images showed parallel and uniform crack formation (Figure S15a,b, Supporting Information), similar to nanosized line patterns. However, larger pattern sizes decreased strain sensitivity due to increased initial resistance (R_0) compared to nanopatterns (Figure S15c, Supporting Information). The highly sensitive SMARTS clearly detects acoustic waves across a broad frequency range (Figure S16, Supporting Information) and demonstrates remarkable cyclic stability, maintaining accurate and precise strain sensing capabilities even after 20 000 cycles under 1% strain (Figure S17, Supporting Information). To ensure consistent and reliable performance during prolonged operation, a PDMS substrate was strategically used. The integration of the PLA/TPU composite with a PDMS substrate enables the sensor to maintain its high sensitivity while providing exceptional long-term stability under cyclic loading. This approach demonstrates the sensor's potential for extended use in applications requiring both precision and durability. Our SMARTS exhibits ultrahigh and stable strain sensing performance, spanning from bio-signal to acoustic wave detection, surpassing previously reported crack-based strain sensors (Figure 2f and Table S1, Supporting Information). This ultrahigh sensitivity stems from the disconnection and reconnection of zip-like cracks in response to strain. Typically, crack-based strain sensors exhibit nonlinear sensitivity due to crack irregularities.[15,23–43,47,48] The rapid increase in resistance occurs when crack recombination due to Poisson's ratio effect is minimized, a critical state manipulated through preset strain. In the lower strain range (1–3 in **Figure 3**a), a slight reduction in the conductive path occurs due to Poisson's ratio effects in the transverse direction relative to the strain direction, leading to minor resistance increases.[23,51] At higher strains (beyond 4), connected regions mostly disconnect, causing significant resistance increase.

2.2. Tunable Sensitivity Induced by Thermo-Responsive Shape Reconfiguration

We employ thermo-responsive shape memory polymer (PLA) to precisely control the preset strain of the sensor, fine-tuning its highly sensitive region for specific applications. This approach overcomes limitations of conventional crack sensors in detecting subtle vibrations at low strains range.[31–36,42] Sensitivity adjustment through shape reconfiguration induced by the shape memory effect offers advantages over existing methods, eliminating the need for separate structural control or complex manufacturing.[37–40] The key to this approach is effectively controlling the initial crack morphology to remain slightly open within the lower strain range. We integrated PLA into the TPU substrate, leveraging its shape memory properties based on entropic elasticity,[52] which refers to the restoring force in stretched chains driven by the tendency to maximize configurational entropy. Thermo-responsive shape memory polymers, such as PLA, contain net points and molecular switches (switching segments) that determine permanent and temporary shapes, respectively.[53] Net points, primarily consisting of crystalline regions, act as physical cross-links that define and maintain the polymer's permanent shape. Elastic energy is primarily stored in the amorphous regions, which allow the polymer to respond to external stress and recover its original shape. Molecular switches, found predominantly in amorphous regions, enable the polymer to adopt

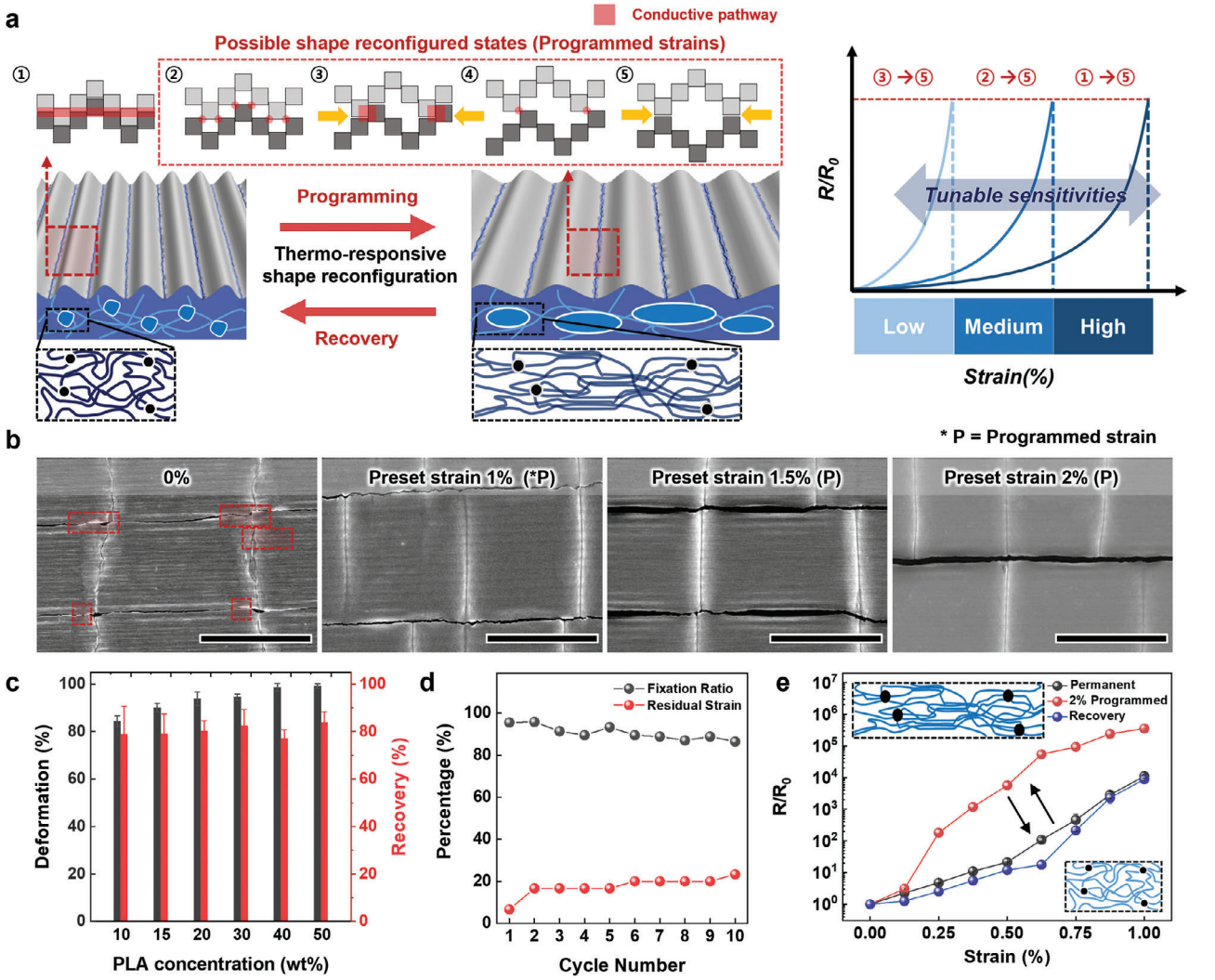

Figure 3. Shape memory-mediated sensitivity tuning through thermal reconfiguration of the crack structures. a) Schematic illustration showing stepwise crack gap modulation through thermo-responsive shape reconfiguration: initial state (1) transforms into various reconfigured states (2–5) with increasing crack gaps via extension and recovery process, where wider gaps result in fewer conductive pathways leading to amplified resistance changes under external strain, enabling tunable sensitivity ranges from low to high strain as shown in resistance–strain curves (right) (b) SEM images of original, shape reconfigured, and fixed states (Shape reconfigured and fixed states at 1%, 1.5%, and 2% strain; Scale bar: 10 μm). c) Deformation and shape recovery ratios for various PLA concentrations in the substrate. Each sensor was stretched to 50% for deformation. Data points represent the average and standard deviation from five samples. d) Shape memory cycle under 50% strain for a sensor with 20 wt% PLA, demonstrating the repeatability of the shape memory effect. e) Tunable sensitivities induced by shape reconfiguration.

temporary shapes. This network structure enables PLA to achieve its shape memory properties.[54]

To activate the shape memory effect, the polymer must be heated above its deformation temperature. Through dynamic mechanical analysis (DMA), the deformation temperature of the PLA/TPU composite was identified as 73 °C, marking the point at which the material transitions to a malleable state. At this temperature, the storage modulus (E') sharply decreases, indicating reduced stiffness, while the loss modulus (E'') peaks due to increased molecular mobility. This result reflects the glass transition temperature (T_g) of PLA in the composite, where polymer chains gain flexibility and enable mechanical deformation (Figure S18, Supporting Information). When heated above the deformation temperature, amorphous segments become malleable, allowing polymer chain alignment under stress. Upon cooling, new physical interactions form between the aligned segments, fixing the temporary shape. During shape recovery, reheating activates the molecular switches, and the stored elastic energy in the amorphous regions drives the polymer to return to its original configuration. This interplay enables PLA to repeatedly transition between permanent and temporary shapes in response to thermal stimuli. This process allows SMARTS to be deformed into desired shapes (Figure S19, Supporting Information). By stretching the sensor to a specific state and cooling it, we establish a new initial crack state through shape reconfiguration. This approach controls the extent of overlap and connected areas in the zip-like cracks of the metal film, enabling customizable initial resistance and precise sensitivity adjustment.

Figure 3b and Figure S20 (Supporting Information) show SEM images of surfaces with open and close cracks. In the original state, cracks are closed with partially connected regions (Figure 3b and Figure S20, Supporting Information, pale red boxes in programmed strain 0%). By controlling crack displacement through heating and cooling of the shape memory PLA/TPU substrate, we modified the ratio of disconnected to reconnected regions, reducing connected areas and consequently increasing initial resistance (Figure 3b and Figure S20, Supporting Information, sample programmed at 1%–2% strains). This demonstrates the sensitivity tuning mechanism, which uses programmed strain to preopen cracks. By reducing the number of conductive pathways at the initial state, this approach amplifies resistance changes even under small deformations, narrowing the sensitive zone and enabling precise control over the sensor's performance. The efficacy of sensitivity tuning via shape reconfiguration depends on the properties of shape fixation and recovery of the substrate. We quantified these properties by measuring shape fixation and recovery ratios. Samples with varying PLA concentrations were subjected to a large tensile strain (50%) and allowed to recover. As the PLA content increased, deformation fixation improved, indicating enhanced shape retention, while the recovery ratio remained consistently around 80%. Notably, composites with 10 wt% PLA demonstrated sufficient fixation and recovery, showing potential for use in high-sensitivity with effective sensitivity tuning (Figure 3c and Figure S21, Supporting Information). In Figure 3d, the residual stress stabilized after the third cycle, indicating that the PLA/TPU composites achieve consistent and reliable shape memory performance after initial conditioning cycles. This stabilization highlights the material's ability to maintain durability and repeatability during multiple deformation and recovery processes, which is critical for long-term applications. The slight changes in residual stress observed during the early cycles could be attributed to the natural settling or alignment of the internal polymer network, suggesting that the material undergoes an initial adaptation phase. This behavior could also be advantageous, as it indicates the material's capacity to stabilize its mechanical properties under repeated cycles. Further exploration of this early adaptation phase may provide insights into optimizing the material for faster stabilization and even higher reliability in practical applications.

The sustainable shape memory property was further validated by analyzing resistance changes in the original, shape-reconfigured, and recovered states. When programmed at a 2% shifted position, the reconfigured sensor exhibited an initial resistance level similar to that of the original sensor stretched by ≈0.5% (Figure S21a, Supporting Information). This behavior indicates that cracks maintained a stretched state, despite slight recovery in the lower strain range. Notably, at subtle strains below 1%, both resistance values and sensitivity significantly increased after shape reconfiguration at various tensile strains (0.5, 1%), subsequently returning to original values. (Figure 3e and Figure S21, Supporting Information). Further investigation under various strains (Figure S22, Supporting Information) suggested that appropriate programming of prestrain enables the adjustment of ultra-sensitive regions, supporting precise control over the sensor's sensitivity in the lower strain range (<1%). Beyond 1% strain, resistance changes reached saturation more quickly as the shape deformation ratio increased, attributed to the rapid crack opening. Sensitivities were effectively tuned and recovered across all tested PLA/TPU weight ratios (Figure S23, Supporting Information), indicating successful crack reconfiguration and fixation. This sensitivity tuning capability enables shifting the ultra-sensitive zone from lower to higher strain ranges, facilitating optimal sensing of target strain. As a result, this approach eliminates the need for multiple devices with varying sensitivities, as sensitivity can be controlled within a single sensor in response to tensile strain. This SMARTS offers both ultrahigh and adjustable sensitivity, suitable for applications requiring detection of subtle changes with heightened sensitivity. This capability transcends ordinary sensing limits, allowing for optimal detection across a broad range of stimuli.

2.3. Multifunctional Sensing Performances in Physiological and Acoustic Detection

The shape reconfigurable crack-based strain sensor, featuring ultrahigh sensitivity and tunable sensitivities, has potential for expanded application in fields requiring detection of subtle strain changes. Arterial pulse waveforms contain crucial cardiovascular information, including systolic and diastolic pressures, essential for comprehensive diagnosis of cardiovascular diseases. The ultrahigh sensitivity of the SMARTS makes it suitable for arterial pulse monitoring when conformally mounted on healthy subjects in their mid-20s. When applied to a subject's wrist (radial artery) and neck (carotid artery), the sensor distinguished P_1 (Incident), P_2 (Tidal), and P_3 (Diastolic) waves of arterial pulses, which allowed calculation of key cardiovascular indices: radial augmentation index ($AI_r = P_2/P_1$), diastolic augmentation index ($DAI_r = P_3/P_1$), and digital volume pulse time ($TDVP = TP_2 - TP_1$), where TP_2 and TP_1 are the times of occurrence of the tidal and incident peaks, respectively. These indices provide valuable information about arterial stiffness and wave reflections, which are important markers of cardiovascular health. Calculated indices (AI_r, DAI_r, and TDVP) based on radial arterial pulse showed values of 0.45, 0.41, and 0.183 s, while those from carotid arterial pulse were 0.46, 0.36, and 0.243 s, respectively (**Figure 4a(i,ii)**). These values were consistent with those expected for a healthy individual in their mid-20s.[55] These noninvasive pulse monitoring capabilities enhance potential for accurate diagnosis of cardiovascular health.

The ultrahigh sensitivity of our sensor enables detection of subtle vibrations induced by acoustic waves, allowing recognition of different sound patterns. We demonstrate this capability by attaching the SMARTS to a speaker and playing "crack sensor" in male and female voices. Compared to microphone-based voice recognition (Figure 4b), the SMARTS showed comparable performance in recognizing and distinguishing sounds. In addition, the SMARTS differentiated between the male and female sound waves, as evidenced by distinct patterns in short-time Fourier transform (STFT) data (Figure 4c,d). The STFT results demonstrate that male voices predominantly exhibit energy concentrated in lower frequency ranges, which appear as narrow and vertically aligned harmonic bands. In contrast, female voices distribute energy across a broader frequency range and exhibit more dynamic amplitude variations. These distinctive patterns arise from physiological differences in

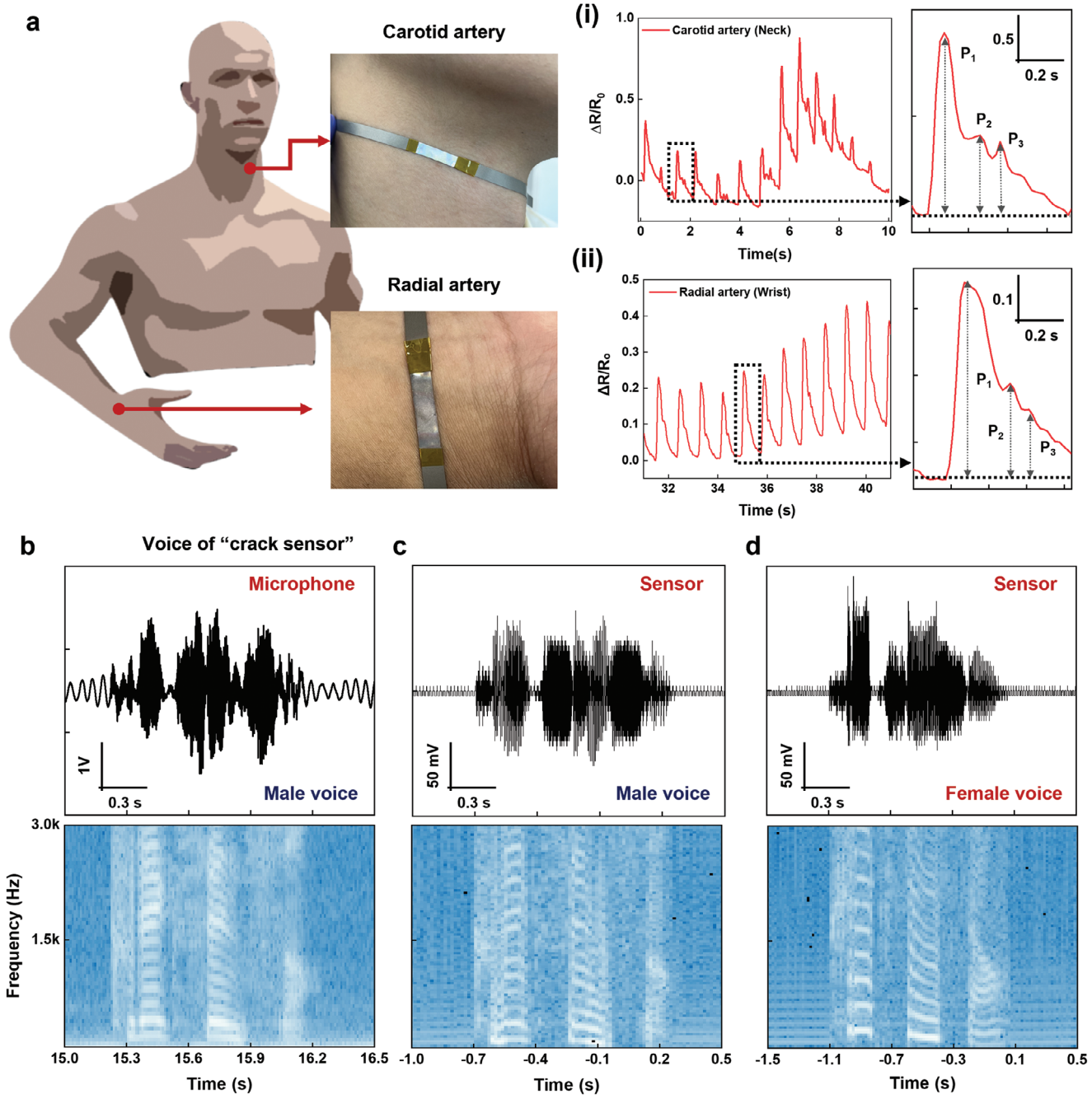

Figure 4. Multifunctional sensing capabilities in physiological and acoustic detection. a) Photographs and schematic illustrations of the wearable crack sensor attached to various body parts for monitoring arterial pulse waves: Carotid artery on the neck (i) and radial artery on the wrist (ii), with corresponding pulse wave signals clearly distinguishing characteristic peaks P_1 (Incident), P_2 (Tidal), and P_3 (Diastolic). b–d) Voice recognition comparison between conventional microphone (b) and crack sensor (c,d), showing time-dependent resistance-induced voltage signals measured by oscilloscope in response to sound vibrations (upper) and corresponding STFT analysis (lower) for each case: male voice recorded with microphone (b), male voice recorded with crack sensor (c), and female voice recorded with crack sensor (d), all saying "Crack sensor".

vocal cord structure and vibration frequency between male and female speakers, resulting in characteristic sound wave patterns that the SMARTS effectively captures. The ability of our SMARTS to capture these subtle differences highlights its potential for advanced acoustic analysis and voice recognition applications.

2.4. Enhanced Acoustic Wave Detection through Shape-Programmable Sensitivity Control

Moreover, the ability of tuning the sensitivity in a single SMARTS extends sound detection capability beyond direct contact with the speaker. It can also detect air vibrations caused by sound

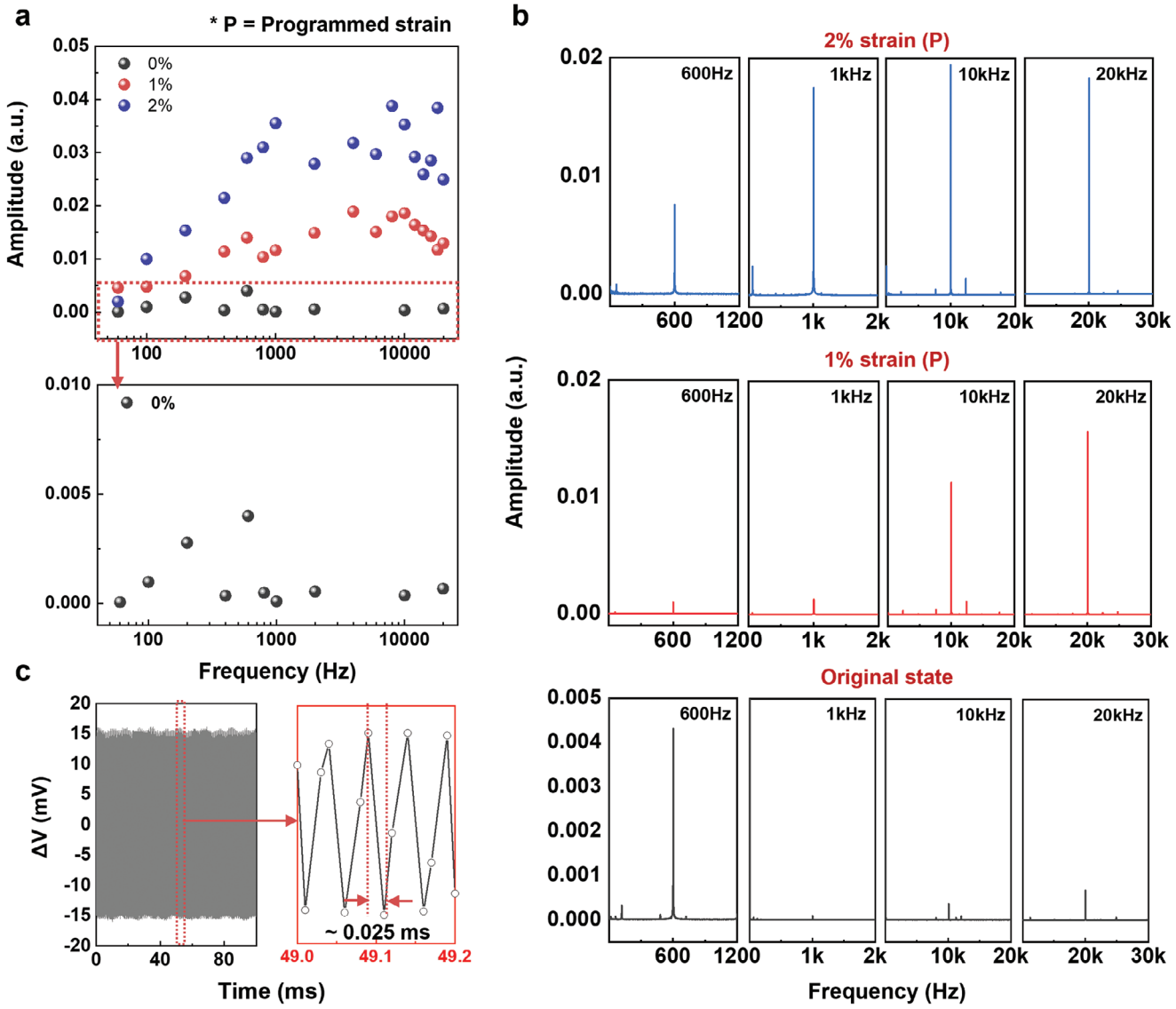

Figure 5. Enhanced acoustic wave detection through shape-programmable sensitivity control. a) Amplitude responses under different preset strains (0%, 1%, and 2%) across frequency range (100 Hz to 20 kHz), with magnified view of original signal (0% strain) shown below for clarity. b) Comparison of frequency sensing amplitudes under different preset strain conditions: 2% (blue, top), 1% strain (red, middle), and original state (black, bottom). c) Demonstration of ultrafast response time (≈0.025 ms) to high frequency acoustic waves (20 kHz).

waves emitted from the speaker at a distance, similar to a microphone, with enhanced performance for sensing target frequencies through shape reconfiguration. To evaluate this capability, we connected a commercial speaker to an oscillator for target frequency generation, measuring resulting waveforms using an oscilloscope (Figure S24, Supporting Information). In this setup, the SMARTS was connected in series with a fixed resistor, and a constant voltage was applied using a sourcemeter. Real-time voltage fluctuations, induced by sound-driven resistance changes, were accurately recorded using the oscilloscope. This approach enabled precise monitoring of high-frequency signals. Leveraging this setup, the SMARTS, installed at a distance from the speaker, demonstrated excellent performance across a wide frequency range (100–20 000 Hz) with a high signal-to-noise (S/N) ratio. Notably, shape reconfiguration-induced preset strains further enhanced target frequency detection, as evidenced by increased amplitudes in response to target frequencies (**Figure** 5a). This enhancement is attributable to the preset strain effectively responding to minimal vibrations by tuning the sensitive region toward a narrower range. The amplitudes increased up to 40 times for target frequencies through this tuning process (Figure 5b and Figure S25, Supporting Information). In addition, the sensor exhibited an ultrafast response time (≈0.025 ms) at high frequencies (20 000 Hz) (Figure 5c).

The tunable sensitivity of a single SMARTS enhances its applicability in strain and minute vibration sensing in contact with sources and extends its capability to precise acoustic wave detection while remaining ultrahigh sensitivity. In its original state, the SMARTS is optimized for tensile strain detection, suitable for applications like pulse monitoring and general strain

sensing including subtle vibrations. When reconfigured by heating, its sensitivity increases dramatically, becoming particularly effective for detecting minute strains, including those produced by sound waves. This adaptability through thermally-induced shape reconfiguration enables the single smart strain sensor to detect a variety of stimuli in their most optimized states. The versatility of this sensor eliminates the need for multiple specialized devices, as it can be adjusted to suit different sensing requirements within a single unit. This unique combination of tunable sensitivity and versatility in a single SMARTS represents a significant advancement in sensor technology, eliminating the need for multiple specialized devices while offering a comprehensive solution for diverse sensing applications ranging from biomedical monitoring to acoustic detection.

3. Conclusion

We have developed a shape-reconfigurable crack-based strain sensor with ultrahigh and tunable sensitivity based on the precise control of nanocrack formation on a shape memory polymer substrate. The sensor design, based on the uniform formation of parallel crack structures guided by nanoscale line patterns, allows for exceptional sensitivity with a GF = 2.7×10^9 at 2% strain. In particular, our sensor can tune its sensitivities through crack width changes by shape reconfiguration of crack structures due to the shape memory effect in the PLA/TPU composite. This feature allows a single sensor to adapt to various sensing requirements by leveraging shape memory functionality, enabling sensitivity adjustments without requiring multiple specialized sensors. This approach reduces complexity by eliminating the need for separate fabrication processes for different sensitivities, streamlining production and enhancing cost-effectiveness and fabrication efficiency. Our sensor demonstrated remarkable versatility in detecting a wide range of stimuli, from subtle biological signals to acoustic waves across a broad frequency spectrum (100–20 000 Hz). In addition, the rapid response time of 0.025 ms, ability to detect strains as low as 0.025%, and stable performance over 20 000 cycles ascertain the potential of our sensor for diverse practical applications. This combination of ultrahigh sensitivity, tunability, and durability positions our sensor as a groundbreaking technology with potential impacts across various fields, including wearable electronics, healthcare monitoring, and human–machine interfaces. The development of a highly sensitive and tunable sensor with shape memory capabilities demonstrates a new paradigm in sensor design, offering promising directions for next-generation smart sensing systems that demand both precision and adaptability.

4. Experimental Section

Materials Preparation: Polylactic acid (PLA; Goodfellow, USA) and thermoplastic polyurethane (TPU; Kolon Plastics, South Korea) were dispersed in N,N-dimethylformamide (DMF, 99.8%, Sigma-Aldrich) at 80 °C with magnetic stirring.

Fabrication of Shape Memory Strain Sensor: The line-patterned PDMS mold was fabricated by casting a 10:1 mixture of PDMS (Sylgard 184, Dow Corning, USA) and curing agent at 80 °C for 2 h. PLA/TPU solution was poured into the line-patterned PDMS mold and annealed in a hot vacuum oven at 150 °C for 2 h. Pt was sputtered onto the PLA/TPU film (5 mm × 15 mm) for 3 min using K575X (EMITECH, South Korea). Cracks were generated along the lines by pre-stretching the Pt sputtered PLA/TPU film using a tensile strain tester (TXA-TM, Yeonjin Corp, South Korea).

Line-Patterned Si Master Mold Fabrication: Line patterns with widths and spacings of 4/8, and 8/16 m were patterned on a Si wafer by photolithography. A 100 nm Cr layer was then deposited by electron-beam evaporation, followed by a lift-off process in acetone. The Cr layer served as an etch mask during the subsequent Si etching process. Si was etched to a depth of 1 m by inductively coupled plasma reactive ion etching (ICP-RIE). The Cr etch mask was removed using a Cr etchant (Sigma-Aldrich).

Characterization of Crack Sensor: Surface morphology was analyzed using field-emission SEM (S-4800 and SU8220, Hitachi, Japan) operating at 10 kV and AFM (Dimension ICON, Bruker Nano Surface, USA) in tapping mode. Optical images of the surface were further examined using an optical microscope (Olympus BX53). The loss factor was measured using DMA (Q800, TA Instruments, USA) at 1 Hz frequency. Raman spectra and mapping were acquired using a confocal Raman microscope (Alpha 300R, WITec, Germany) with 532 nm laser excitation. Stress-strain curves were obtained using a tensile strain tester (TXA-TM, Yeonjin Corp, South Korea) at 0.01 and 0.1 mm s^{-1} rates.

Evaluation of Shape Memory Characteristics: The shape memory behavior of the sample was assessed through sequential deformation, fixation, and recovery processes. To induce deformation, the sample was securely fastened onto a heating plate using PI tape and heated to a temperature above its glass transition temperature (Tg), as monitored using a portable IR camera (E54, FLIR, USA). Upon reaching the target temperature, the sample was stretched to 50% of its initial length and held in this elongated state. The deformed shape was fixed by allowing the sample to cool to room temperature while maintaining the applied strain. The fixed configuration was preserved until the sample was reheated above Tg. The final fixed length was measured using a portable optical microscope (HA010, Gasworld, South Korea). For the recovery process, the sample was heated to 80 °C for 10 seconds, enabling it to regain its original shape and effectively validating its shape memory performance.

Electrical Measurement of Shape Memory Strain Sensor: The electrical resistance changes were analyzed by a probe station (8000, MS Tech) according to tensile strain controlled by a bending tester (JIBT-100, Junil Tech, South Korea). For shape reconfiguration, the sensor was heated using a heater, and the temperature was measured by an IR camera. Acoustic waves were supplied through a commercial speaker (CS-5100, PILLAR) connected to an oscillator (SG-3428B, Sigma Eltec) and measured using an oscilloscope (DPO 220B, Tektronix, USA) with a voltage bias supplied by a sourcemeter (S-2400, Keithley).

Supporting Information

Supporting Information is available from the Wiley Online Library or from the author.

Acknowledgements

S.L. and Y.L. contributed equally to this work. This work was supported by the National Research Foundation (NRF) of Korea (2021R1A2C3009222, 2022M3H4A1A02076825) and National Research Council of Science and Technology (NST) grant by the Korea government (MSIT) (No. CAP22083-201).

Conflict of Interest

The authors declare no conflict of interest.

Data Availability Statement

The data that support the findings of this study are available from the corresponding author upon reasonable request.

Keywords

parallel nanocrack, shape memory polymer, shape-reconfigurable strain sensor, tunable sensitivity, ultrahigh gauge factor

Received: November 11, 2024
Revised: December 31, 2024
Published online:

[1] G. Y. Bae, S. W. Pak, D. Kim, G. Lee, D. H. Kim, Y. Chung, K. Cho, *Adv. Mater.* **2016**, *28*, 5300.
[2] J. H. Koo, S. Jeong, H. J. Shim, D. Son, J. Kim, D. C. Kim, S. Choi, J.-I. Hong, D.-H. Kim, *ACS Nano* **2017**, *11*, 10032.
[3] K. Song, S. H. Kim, S. Jin, S. Kim, S. Lee, J.-S. Kim, J.-M. Park, Y. Cha, *Sci. Rep.* **2019**, *9*, 8988.
[4] H. Kim, Y.-T. Kwon, H.-R. Lim, J.-H. Kim, Y.-S. Kim, W.-H. Yeo, *Adv. Funct. Mater.* **2021**, *31*, 2005692.
[5] C. Pang, J. H. Koo, A. Nguyen, J. M. Caves, M.-G. Kim, A. Chortos, K. Kim, P. J. Wang, J. B.-H. Tok, Z. Bao, *Adv. Mater.* **2015**, *27*, 634.
[6] M. Liu, X. Pu, C. Jiang, T. Liu, X. Huang, L. Chen, C. Du, J. Sun, W. Hu, Z. L. Wang, *Adv. Mater.* **2017**, *29*, 1703700.
[7] J. Kim, M. Lee, H. J. Shim, R. Ghaffari, H. R. Cho, D. Son, Y. H. Jung, M. Soh, C. Choi, S. Jung, K. Chu, D. Jeon, S.-T. Lee, J. H. Kim, S. H. Choi, T. Hyeon, D.-H. Kim, *Nat. Commun.* **2014**, *5*, 5747.
[8] M. Liu, X. Pu, C. Jiang, T. Liu, X. Huang, L. Chen, C. Du, J. Sun, W. Hu, Z. L. Wang, *ACS Nano* **2017**, *29*, 1703700.
[9] Y. Lee, J. Park, S. Cho, Y.-E. Shin, H. Lee, J. Kim, J. Myoung, S. Cho, S. Kang, C. Baig, H. Ko, *ACS Nano* **2018**, *12*, 4045.
[10] J. Kim, M. Jang, G. Jeong, S. Yu, J. Park, Y. Lee, S. Cho, J. Yeom, Y. Lee, A. Choe, Y.-R. Kim, Y. Yoon, S. S. Lee, K.-S. An, H. Ko, *Nano Energy* **2021**, *89*, 106409.
[11] J.-H. Lee, Y.-N. Kim, J. Lee, J. Jeon, J.-Y. Bae, J.-Y. Lee, K.-S. Kim, M. Chae, H. Park, J.-H. Kim, K.-S. Lee, J. Kim, J. K. Hyun, D. Kang, S.-K. Kang, *Sci. Adv.* **2024**, *10*, eads9258.
[12] K. Kwon, J. U. Kim, S. M. Won, J. Zhao, R. Avila, H. Wang, K. S. Chun, H. Jang, K. H. Lee, J.-H. Kim, S. Yoo, Y. J. Kang, J. Kim, J. Lim, Y. Park, W. Lu, T.-i. Kim, A. Banks, Y. Huang, J. A. Rodgers, *Nat. Biomed. Eng.* **2023**, *7*, 1215.
[13] D.-S. Kim, Y. W. Choi, A. Shamugasundaram, Y.-J. Jeong, J. Park, N.-E. Oyunbaatar, E.-S. Kim, M. Choi, D.-W. Lee, *Nat. Commun.* **2020**, *11*, 535.
[14] A. Abramson, C. T. Chan, Y. Khan, A. Mermin-Bunnell, N. Matsuhisa, R. Fong, R. Shad, W. Hiesinger, P. Mallick, S. S. Gambhir, Z. Bao, *Sci. Adv.* **2022**, *8*, eabn6550.
[15] T.-S. D. Le, J. An, Y. Huang, Q. Vo, J. Boonruangkan, T. Tran, S.-W. Kim, G. Sun, Y.-J. Kim, *ACS Nano* **2019**, *13*, 13293.
[16] C. M. Boutry, M. Nerge, M. Jorda, O. Vardoulis, A. Chortos, O. Khatib, Z. Bao, *Sci. Robot.* **2018**, *3*, eaau6914.
[17] S. Baek, Y. Lee, J. Baek, J. Kwon, S. Kim, S. Lee, K.-P. Strunk, S. Stehlin, C. Melzer, S.-M. Park, H. Ko, S. Jung, *ACS Nano* **2022**, *16*, 368.
[18] X.-M. Wang, L.-Q. Tao, M. Yuan, Z.-P. Wang, J. Yu, D. Xie, F. Luo, X. Chen, C. P. Wong, *Nat. Commun.* **2021**, *12*, 1776.
[19] Y. Lee, J. Myoung, S. Cho, J. Park, J. Kim, H. Lee, Y. lee, S. Lee, C. Baig, H. Ko, *ACS Nano* **2021**, *15*, 1795.
[20] J. Park, M. Kim, Y. Lee, H. S. Lee, H. Ko, *Sci. Adv.* **2015**, *1*, e1500661.
[21] K. Takei, Z. Yu, M. Zheng, H. Ota, T. Takahashi, A. Javey, *Proc. Natl. Acad. Sci. USA* **2014**, *111*, 1703.
[22] C. Chen, X.-L. Li, S. Zhao, Y. Song, Y. B. Zhu, Q. Wang, C. Zhong, R. Chen, E. Li, Z. Li, J.-W. Liu, *Device* **2023**, *1*, 100148.
[23] D. Kang, P. V. Pikhitsa, Y. W. Choi, C. Lee, S. S. Shin, L. Piao, B. Park, K.-Y. Suh, T.-I. Kim, M. Choi, *Nature* **2014**, *516*, 222.
[24] B. Park, J. Kim, D. Kang, C. Jeong, K. S. Kim, J. U. Kim, P. J. Yoo, T.-I. Kim, *Adv. Mater.* **2016**, *28*, 8130.
[25] L. Liu, S. Niu, J. Zhang, Z. Mu, J. Li, B. Li, X. Meng, C. Zhang, Y. Wang, T. Hou, Z. Han, S. Yang, L. Ren, *Adv. Mater.* **2022**, *34*, 2200823.
[26] J. Wang, L. Liu, C. Yang, C. Zhang, B. Li, X. Meng, G. Ma, D. Wang, J. Zhang, S. Niu, J. Zhao, Z. Han, Z. Yao, L. Ren, *ACS Appl. Mater. Interfaces* **2022**, *14*, 16885.
[27] J.-H. Lee, J.-Y. Bae, Y.-N. Kim, M. Chae, W.-J. Lee, J. Lee, I.-D. Kim, J. K. Hyun, K.-S. Lee, D. Kang, S.-K. Kang, *Adv. Funct. Mater.* **2024**, *34*, 2406035.
[28] H. Jeon, S. K. Hong, M. S. Kim, S. J. Cho, G. Lim, *ACS Appl. Mater. Interfaces* **2017**, *9*, 41712.
[29] Y. Yang, L. Shi, Z. Cao, R. Wang, J. Sun, *Adv. Funct. Mater.* **2019**, *29*, 1807882.
[30] R. Rahimi, M. Ochoa, W. Yu, B. Ziaie, *ACS Appl. Mater. Interfaces* **2015**, *7*, 4463.
[31] Y.-F. Wang, T. Sekine, Y. Takeda, J. Hong, A. Yoshida, H. Matsui, D. Kumaki, T. Nishikawa, T. Shiba, T. Sunaga, S. Tokito, *ACS Appl. Mater. Interfaces* **2020**, *12*, 35282.
[32] J. Shu, R. Yang, Y. Chang, X. Guo, X. Yang, *J. Alloys Compd.* **2021**, *879*, 160466.
[33] Z. Chu, W. Jiao, Y. Huang, Y. Zheng, R. Wang, X. He, *J. Mater. Chem. A* **2021**, *9*, 9634.
[34] W. Miao, Y. Yao, Z. Zhang, C. Ma, S. Li, J. Tang, H. Liu, Z. Liu, D. Wang, M. A. Camburn, J.-C. Fang, R. Hao, X. Fang, S. Zheng, N. Hu, X. Wang, *Nat. Commun.* **2019**, *10*, 3862.
[35] K.-H. Kim, S. K. Hong, S.-H. Ha, L. Li, H. W. Lee, J.-M. Kim, *Mater. Horiz.* **2020**, *7*, 2662.
[36] Y. Zhang, Y. Xiao, Y. Xu, S. Zhang, C. Qu, H. Liu, K. Huang, H. Shao, *ACS Appl. Mater. Interfaces* **2023**, *15*, 31729.
[37] J. Zhu, X. Wu, J. Jan, S. Du, J. Evans, A. C. Arias, *ACS Appl. Mater. Interfaces* **2021**, *13*, 38105.
[38] K. K. Kim, I. Ha, M. Kim, J. Choi, P. Won, S. Jo, S. H. Ko, *Nat. Commun.* **2020**, *11*, 2149.
[39] Y. Jiang, Q. He, J. Cai, D. Shen, X. Hu, D. Zhang, *ACS Appl. Mater. Interfaces* **2020**, *12*, 58317.
[40] T. Kim, I. Hong, Y. Roh, D. Kim, S. Kim, S. Im, C. Kim, K. Jang, S. Kim, M. Kim, J. Park, D. Gong, K. Ahn, J. Lee, G. Lee, H.-S. Lee, J. Kang, J. M. Hong, S. Lee, S. Seo, B.-K. Koo, J.-S. Koh, S. Han, D. Kang, *npj Flexible Electron.* **2023**, *7*, 12.
[41] M. D. Thouless, Z. Li, N. J. Douville, S. Takayama, *J. Mech. Phys. Solids* **2011**, *59*, 1927.
[42] W. Wang, L. Lu, Z. Li, L. Lin, Z. Liang, X. Lu, Y. Xie, *ACS Appl. Mater. Interfaces* **2022**, *14*, 1315.
[43] S. Yang, W. Yang, R. Yin, H. Liu, H. Sun, C. Pan, C. Liu, C. Shen, *Chem. Eng. J.* **2022**, *437*, 135377.
[44] Y. Xin, J. Zhou, X. Xu, G. Lubineau, *Nanoscale* **2017**, *9*, 10897.
[45] Z. Han, L. Liu, J. Zhang, Q. Han, K. Wang, H. Song, Z. Wang, Z. Jiao, S. Niu, L. Ren, *Nanoscale* **2018**, *10*, 15178.
[46] F. Spaepen, *Acta Mater.* **2000**, *48*, 31.
[47] T. Yang, X. Li, X. Jiang, S. Lin, J. Lao, J. Shi, Z. Zhen, Z. Li, H. Zhu, *Mater. Horiz.* **2016**, *3*, 248.
[48] Q. Zou, J. Zheng, Q. Su, W. Qang, W. Gao, Z. Ma, *Sens. Actuators, A* **2019**, *300*, 111658.
[49] K. H. Nam, I. H. Park, S. H. Ko, *Nature* **2012**, *485*, 221.
[50] M. F. Ahmed, Y. Li, Z. Yao, K. Cao, C. Zeng, *J. Appl. Polym. Sci.* **2019**, *136*, 47416.
[51] H. Sun, C. Ye, G. Zhao, H. Zhang, Z. Liu, W. Dai, J. Wang, F. E. Alam, Q. Yan, X. Li, J. Xu, C.-Y. Chen, P. Zhao, J. Ye, N. Jiang, D. Chen, S. Wu, J. Kong, C.-T. Lin, *J. Mater. Chem. A* **2020**, *8*, 10310.
[52] M. Behl, A. Lendlein, *Mater. Today* **2007**, *10*, 20.
[53] J. Delaey, P. Dubruel, S. V. Vlierberghe, *Adv. Funct. Mater.* **2020**, *30*, 1909047.
[54] M. Mehrpouya, H. Vahabi, S. Janbaz, A. Darafsheh, T. R. Mazur, S. Ramakrishna, *Polymer* **2021**, *230*, 124080.
[55] W. W. Nichols, *Am. J. Hypertens.* **2005**, *18*, 3.

